

## Histological and molecular classifications of pediatric glioma with time-dependent diffusion MRI-based microstructural mapping

Hongxi Zhang<sup>†</sup>, Kuiyuan Liu<sup>†</sup>, Ruicheng Ba, Zelin Zhang, Yi Zhang, Ye Chen, Weizhong Gu, Zhipeng Shen, Qiang Shu, Junfen Fu, and Dan Wu<sup>✉</sup>

*Department of Radiology, Children's Hospital, Zhejiang University School of Medicine, National Clinical Research Center for Child Health, Hangzhou, China (H.Z., D.W.); Department of Biomedical Engineering, College of Biomedical Engineering & Instrument Science, Zhejiang University, Hangzhou, China (K.L., R.B., Z.Z., Y.Z., D.W.); Children's Hospital, Zhejiang University School of Medicine, National Clinical Research Center for Child Health, Hangzhou, China (Y.C.); Department of Pathology, Children's Hospital, Zhejiang University School of Medicine, National Clinical Research Center for Child Health, Hangzhou, China (W.G.); Department of Neurosurgery, Children's Hospital, Zhejiang University School of Medicine, National Clinical Research Center for Child Health, Hangzhou, China (Z.S.); Department of Cardiology, Children's Hospital, Zhejiang University School of Medicine, National Clinical Research Center for Child Health, Hangzhou, China (Q.S.); Department of Endocrinology, Children's Hospital, Zhejiang University School of Medicine, National Clinical Research Center for Child Health, Hangzhou, China (J.F.)*

<sup>†</sup>These authors contributed equally to this work.

Corresponding Author: Dan Wu, PhD, Department of Biomedical Engineering, Zhejiang University, Room 525, Zhou Yiqing Building, Yuquan Campus, Zhejiang University, Hangzhou, 310027, China ([danwu.bme@zju.edu.cn](mailto:danwu.bme@zju.edu.cn)); Junfen Fu, MD, PhD, Department of Endocrinology, Children's Hospital, Zhejiang University School of Medicine, National Clinical Research Center for Child Health, Hangzhou, China ([fjf68@zju.edu.cn](mailto:fjf68@zju.edu.cn)).

### Abstract

**Background.** Gliomas are the most common type of central nervous system tumors in children, and the combination of histological and molecular classification is essential for prognosis and treatment. Here, we proposed a newly developed microstructural mapping technique based on diffusion-time-dependent diffusion MRI  $t_d$ -dMRI theory to quantify tumor cell properties and tested these microstructural markers in identifying histological grade and molecular alteration of H3K27.

**Methods.** This prospective study included 69 pediatric glioma patients aged  $6.14 \pm 3.25$  years old, who underwent  $t_d$ -dMRI with pulsed and oscillating gradient diffusion sequences on a 3T scanner. dMRI data acquired at varying  $t_d$ s were fitted into a 2-compartment microstructural model to obtain intracellular fraction ( $f_{in}$ ), cell diameter, cellularity, etc. Apparent diffusivity coefficient (ADC) and T1 and T2 relaxation times were also obtained. H&E stained histology was used to validate the estimated microstructural properties.

**Results.** For histological classification of low- and high-grade pediatric gliomas, the cellularity index achieved the highest area under the receiver-operating-curve (AUC) of 0.911 among all markers, while ADC, T1, and T2 showed AUCs of 0.906, 0.885, and 0.886. For molecular classification of H3K27-altered glioma in 39 midline glioma patients, cell diameter showed the highest discriminant power with an AUC of 0.918, and the combination of cell diameter and extracellular diffusivity further improved AUC to 0.929. The  $t_d$ -dMRI estimated  $f_{in}$  correlated well with the histological ground truth with  $r = 0.7$ .

**Conclusions.** The  $t_d$ -dMRI-based microstructural properties outperformed routine MRI measurements in diagnosing pediatric gliomas, and the different microstructural features showed complementary strength in histological and molecular classifications.

### Key Points

- We proposed a new microstructural imaging technique to quantify tumor pathology.
- It classified low- and high-grade pediatric gliomas using cellularity index (AUC = 0.91), and H3K27-altered and wildtype using cell diameter (AUC = 0.92), outperforming conventional MRI.

### Importance of the Study

The current study targeted histological and molecular classifications of pediatric gliomas. In a cohort of 69 pediatric glioma patients in this preliminary study, the proposed tumor microstructural markers obtained from diffusion-time-dependent diffusion MRI  $t_d$ -dMRI demonstrated promising diagnostic power in differentiating low- versus high-grade glioma with an AUC of 0.911 using the cellularity index, as well as H3K27-altered versus wildtype with an AUC of 0.918 based on the cell diameter measurement, outperforming the conventional apparent diffusion coefficient or T1/T2 relaxation time measurements.

Given that the combination of histological and molecular classification is essential for precise prognosis and optimal treatment plan in central nervous system (CNS) tumor patients, as pointed out by the WHO 2021 guideline, we think the high diagnostic performance of  $t_d$ -dMRI based microstructural markers in both histological and molecular classification makes it potentially useful not only in pediatric gliomas but also in adult types of gliomas and other types of CNS tumors. The 6 min protocol is easily translatable to routine clinical scans.

Central nervous system (CNS) tumors are the most frequent solid tumors in children, accounting for 21% of pediatric cancers and representing a primary cause of mortality.<sup>1</sup> Survivors of pediatric CNS tumors are at high risk for late mortality and for developing life-long neurological and chronic diseases.<sup>2</sup> Gliomas are the most common type of CNS tumors, accounting for 35% of CNS tumors diagnosed in children between birth and 19 years of age.<sup>1</sup> Pediatric gliomas are typically classified into histologically low-grade glioma (LGG) accounts for the majority of pediatric glioma and ensures a favorable prognosis with more than 90% overall survival rate; and high-grade glioma (HGG) inflect about one-third of the population and has less than 10% long-term survival rate, despite the aggressive treatment regimens.<sup>3,4</sup> Therefore, accurate histological classification is important for prognostic decisions and management strategy.

Among pediatric gliomas, midline glioma is a common type, and given the special location of midline glioma in the thalamus, brainstem, or spinal cord, it is often considered nonoperative and faces a very poor survival rate.<sup>5</sup> In pediatric midline gliomas, the H3K27-altered patients suffered significantly shorter overall survival than wildtypes, regardless of histologic features.<sup>6</sup> Therefore, H3K27-alteration has been defined as the most important molecular marker for midline glioma in the 2021 World Health Organization (WHO) classification of tumors of CNS<sup>7</sup> and may provide a novel target for radiation and/or immunotherapy.<sup>8</sup> Although H3K27-alteration can be identified from biopsy, the procedure remains very restricted due to the location in the middle deep structures of the brain, as well as the potential bias of biopsy due to the

lack of spatial information in contrast to the molecular heterogeneity.<sup>9</sup>

In an effort to noninvasively identify the histological grade and molecular subtypes of pediatric gliomas before surgery, multiparametric MRI has been commonly used to assist in the diagnosis. Contrast-enhanced T1-weighted MRI is a radiological standard for tumor screening but the degree of enhancement does not always correlate with tumor grade. Diffusion MRI (dMRI) has been shown to outperform conventional MRI, eg, the apparent diffusivity coefficients (ADC) provided good diagnostic power for differentiating HGG from LGG for both pediatric<sup>10</sup> and adult<sup>11</sup> types. Despite its sensitivity advantage, ADC is only a simple measure of restricted diffusivity that is affected by a number of pathological events, such as inflammation, cell proliferation, necrosis or apoptosis, and thus, could not offer specific microstructural information about tumor pathology. Moreover, in an era of molecular diagnostics, the role of dMRI remains very limited. Two recent studies<sup>12,13</sup> reported no statistical difference in ADC between H3K27M-mutant and wild-type midline glioma. An adult glioma study found a marginal ADC difference ( $P = .04$ ) between H3K27M-mutant and wild-type groups.<sup>14</sup>

Recent advances in dMRI-based microstructural imaging provided an opportunity to characterize tumor pathology in vivo. Particularly, besides the  $q$ -space dMRI approaches<sup>15–18</sup> that target fiber/neurite microstructure, diffusion-time dependent dMRI  $t_d$ -dMRI has shown unique advantages in mapping the cellular microstructures by capturing the behavior of restriction diffusion at varying  $t_d$  using a combination of specialized diffusion encoding schemes.<sup>19</sup> The  $t_d$ -dependent diffusion behavior can be

utilized to build biophysical models for quantifying microstructural properties such as cell size, cell volume fraction, and transcytolemmal water exchange.<sup>20–23</sup> The principle of  $t_d$ -dMRI is illustrated in [Supplementary Figure S1](#). In addition to the validation studies in animal models of the tumor,<sup>24</sup> technical feasibility of  $t_d$ -dMRI has been recently tested in head and neck tumors,<sup>25</sup> breast cancer,<sup>21</sup> prostate cancer grade,<sup>26</sup> etc.  $t_d$ -dMRI based microstructural mapping is considered 1 step further toward achieving “virtual pathology,”<sup>27</sup> although the clinical value of this method is still under investigation.

Given the distinct histological signatures between LGG and HGG, eg, anaplastic astrocytoma and glioblastoma exhibit greater cellularity and multiple mitotic figures compared to low-grade astrocytoma,<sup>28</sup> we expect that they are separable with  $t_d$ -dMRI. Moreover, the pathological features of midline glioma with H3K27-alteration, eg, astrocytic morphology that is limited to neoplastic cells,<sup>29</sup> may also allow us to identify the molecular alterations with  $t_d$ -dMRI. Therefore, the aim of the present study is to investigate the clinical value of  $t_d$ -dMRI-based microstructural mapping for noninvasively differentiating the histological grade and molecular alteration of H3K27, both of which are essential in clinical decisions of pediatric glioma.

## Material and Methods

### Patient Cohort

Seventy-five pediatric patients were prospectively recruited between November 2019 and March 2022. The

study was approved by the hospital research ethics board. Written informed consent was obtained from the legal guardians of all participants. The inclusion criteria were as follows: (1) suspected of gliomas, (2) <18 years old, (3) no prior treatment related to gliomas, and (4) eligible for MRI. The exclusion criteria and participation flowchart are illustrated in [Figure 1](#).

### Data Acquisition

All scans were performed on a 3T scanner (Achieva, Phillips Healthcare, Best, The Netherlands) with a maximum gradient of 80 mT/m and slew rate of 200 mT/m/s, and a 24-channel head coil.  $t_d$ -dMRI was acquired using an in-house oscillating gradient spin-echo (OGSE) sequence with trapezoid cosine gradient<sup>30</sup> and pulsed gradient spin-echo (PGSE) sequence. Schematics of OGSE and PGSE sequences are illustrated in [Supplementary Figure S2](#). OGSE data were acquired at 17 Hz (effective  $t_d = 14.7$  ms, 1 cycle,  $b = 500/1000/1500$  s/mm<sup>2</sup>), 33 Hz (effective  $t_d = 7.6$  ms, 2 cycles,  $b = 500$  s/mm<sup>2</sup>), and 50 Hz (effective  $t_d = 5$  ms, 3 cycles,  $b = 350$  s/mm<sup>2</sup>). PGSE was acquired with diffusion duration/separation = 60/82.3 ms at  $b$ -value of 500/1000/1500 s/mm<sup>2</sup>. The other acquisition parameters were kept the same between the two sequences: Echo time/repetition time = 168/3000 ms, field-of-view = 180 × 180 mm, matrix size = 128 × 128, slice thickness = 8 mm, 3 slices, 1 non-diffusion-weighted image (b0), 6 diffusion directions per  $b$ -value, and SENSE acceleration factor = 2. The total scan time of the  $t_d$ -dMRI protocol was 6 min and 19s.

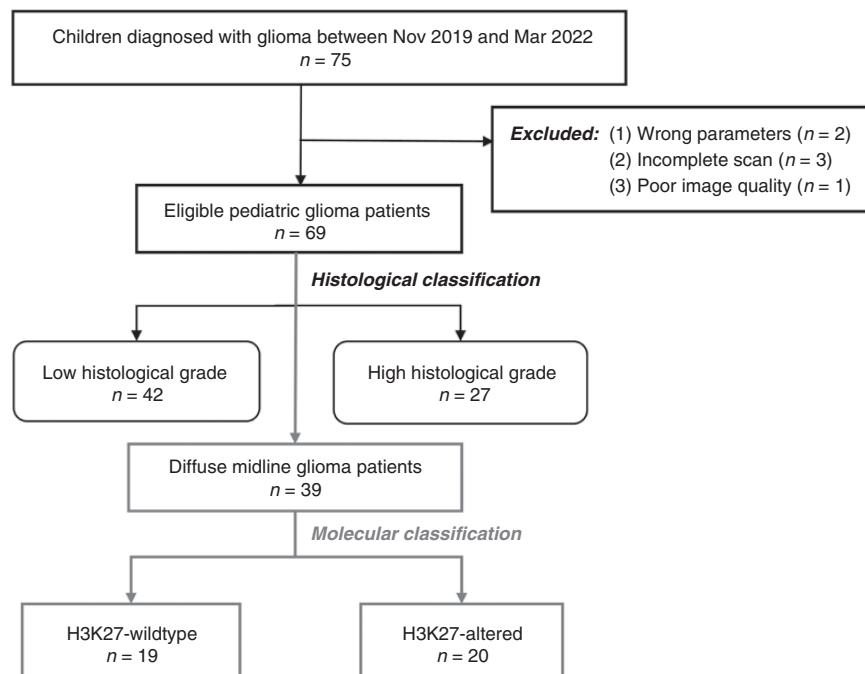


**Figure 1.** The participant enrollment flowchart.

Routine structural MRI included T1-weighted images before and after Gd-enhancement, T2-weighted, and FLAIR images. Quantitative T1 and T2 mapping were obtained using vendor-provided “MIX” sequence,<sup>31</sup> which was acquired using interleaved spin-echo and inversion-recovery sections at a single slice corresponding to the center slice of the  $t_d$ -dMRI scans. The imaging parameters are listed in [Supplementary Table S1](#).

## Image Analysis

To correct for the patient motion and eddy-current-induced image misalignment, we registered all the OGSE images to PGSE according to the  $b_0$  images or diffusion-weighted images at equivalent  $b$ -values in FSL (<https://fsl.fmrib.ox.ac.uk/fsl/fslwiki/FLIRT/>). Registration quality was manually checked by a radiologist (Z.H. with 14 years of experience in pediatric radiology).

$t_d$ -dMRI signals were fitted according to the IMPULSED (Imaging Microstructural Parameters Using Limited Spectrally Edited Diffusion) model,<sup>20</sup> which is a 2-compartment model consisting of the intra- and extra-cellular components:

$$S = f_{in}S_{in} + (1 - f_{in})S_{ex} \quad (1)$$

where  $S$  is the measured  $t_d$ -dMRI signal,  $S_{in}$  and  $S_{ex}$  are the intracellular and extracellular signals, respectively, and  $f_{in}$  represents the volume fraction of the intracellular space. The analytic expression of  $S_{in}$  is defined for spheres<sup>32</sup> based on the diameter and intracellular diffusivity and is adapted for trapezoid OGSE waveform according to.<sup>21</sup>  $S_{ex} = e^{-bD_{ex}}$  considering that the extracellular signal is independent of  $t_d$  within the short  $t_d$  regime,<sup>20</sup> where  $D_{ex}$  is the extracellular diffusivity.

Microstructural parameters including cell diameter  $d$ ,  $f_{in}$ , and  $D_{ex}$  were estimated from Eq. 1 using a nonlinear least squares algorithm in Matlab R2018a (Mathworks, Natick, MA) with a fixed intracellular diffusion coefficient at  $1.0 \mu\text{m}^2/\text{ms}$ . The fitting was repeated 100 times with randomized initializations to avoid local minimums, under the following physiological constraints:  $1 < d < 60 \mu\text{m}$ ,  $0.01 < f_{in} < 1$ ,  $0.5 < D_{ex} < 3.5 \mu\text{m}^2/\text{ms}$ . Cellularity was defined as  $f_{in}/d^3 \times 100$  for simplicity.<sup>26</sup> ADC maps were calculated at each  $t_d$  according to the log-linear fitting  $S/S_0 = e^{-bD}$  to obtain  $D_{0\text{Hz}}$  (PGSE),  $D_{17\text{Hz}}$ ,  $D_{33\text{Hz}}$ , and  $D_{50\text{Hz}}$ . Fractional anisotropy (FA), axial diffusivity (AD), and radial diffusivity (RD) maps were also obtained based on diffusion tensor decomposition using the PGSE data. The Matlab code in a graphic-user interface format was deposited at [https://github.com/KuiyuanLiu/app\\_IMPULSED\\_Fitting](https://github.com/KuiyuanLiu/app_IMPULSED_Fitting).

Based on the MIX data, T1, T2, and proton density maps were obtained simultaneously by solving the interleaved spin-echo and inversion-recovery signal equations with ratios and nonlinear least squares algorithm.<sup>31</sup>

## Histopathological Analysis

Tumor grading was determined according to the 2021 WHO classification of CNS tumors.<sup>7</sup> H3K27-alteration

was determined by immunohistochemical staining using anti-histone H3 (mutated K27M, rabbit monoclonal, clone EPR18340, 1:100, Abcam, Cambridge, UK),<sup>29</sup> performed on a Leica Biosystems BOND3 instrument. The positive status was defined as nuclear staining in >80% of tumor cells visualized in the absence of staining in tumor vascular epithelial cells (internal negative control). The primary antibodies were incubated overnight at 4°C. All sections were counterstained with hematoxylin. All biopsy specimens and histopathological slides were interpreted by a dedicated pathologist (G.W. with 26 years of experience in pathology).

High-definition (30x) hematoxylin and eosin (H&E)-stained sections of suspected glioma tissues were obtained from 37 patients. The nuclei in each H&E section were segmented via a pre-trained Conditional Generative Adversarial Networks (cGAN)<sup>33</sup> (code deposited at [https://github.com/zjuzzl/Prostate\\_MRI/blob/main/Histology.rar](https://github.com/zjuzzl/Prostate_MRI/blob/main/Histology.rar)). The nuclei diameter  $d_{nuclei}$  was calculated for each nucleus as  $d_{nuclei} = 2\sqrt{\frac{A_{nuclei}}{\pi}}$ , where,  $A_{nuclei}$  was the area of the segmented nuclei. Since  $d_{nuclei}$  was obtained from the 2D H&E slices, we adjusted it to a 3D volume-weighted diameter as  $d'_{nuclei} = \sum_n d_{nuclei}^4 / \sum_n d_{nuclei}^3$  where  $n$  represented the nuclei number. The pathology-based  $f_{in} = \left( \sum_n A_{nuclei} / A_{tissue} \right)^{3/2}$ , where,  $A_{tissue}$  was the area of the whole tissue.

## Statistical Analysis

The tumor region-of-interest (ROI) was manually delineated to include both the enhancing and non-enhancing solid components of the tumors, excluding the peritumoral edema, intratumoral hemorrhage, necrosis, calcification, and associated cysts. The ROIs were identified by a dedicated radiologist (Z.H with 14 years of experience in pediatric radiology) on all slices of the  $b_0$  images, T1 and T2 mapping images, and contrast-enhanced T1-weighted images. The tumor volumes were calculated using the ROIs on the T1-weighted images that covered the entire tumor. T1 and T2 relaxation times,  $f_{in}$ ,  $d$ , cellularity,  $D_{ex}$ ,  $D_{0\text{Hz}}$ ,  $D_{17\text{Hz}}$ ,  $D_{33\text{Hz}}$ , and  $D_{50\text{Hz}}$  were averaged from the corresponding ROIs from each patient. Group comparison between LGG and HGG groups and also between H3K27-altered and wildtype groups were performed using a  $t$ -test with unequal variance in Graphpad Prism 8.0 (<https://www.graphpad.com/scientific-software/prism/>). The diagnostic performance of individual MRI metrics and their combinations were evaluated based on accuracy, sensitivity, specificity, and AUC in Graphpad. The correlation between histologically quantified and  $t_d$ -dMRI-fitted microstructural parameters were assessed by linear regression. The significance level was set at  $P = .05$  for all tests.

## Results

### Patient Characteristics

According to the histological examination, 69 pediatric glioma patients were classified into the LGG group ( $n = 42$ )



and HGG group ( $n=27$ ). The midline glioma patients ( $n=39$ ) were further divided into H3K27-altered ( $n=20$ ) and wildtype ( $n=19$ ) according to the immunohistochemical staining. The participant information and tumor characteristics are described in [Supplementary Table S2](#). The tumor volumes were  $22.5 \pm 12.4 \times 10^3 \text{ mm}^3$  based on the T1w-enhanced images.

### Histological Grading

The  $t_d$ -dMRI-based microstructural maps were illustrated in [Figure 2A](#) for 2 representative patients with LGG (3 years old boy, pilocytic astrocytoma, grade 2) and HGG (9 years old boy, midline glioma, grade 4). The ADC maps at individual  $t_d$ s showed a  $t_d$ -dependent increase of ADC from  $D_{0\text{Hz}}$  to  $D_{50\text{Hz}}$  in both LGG and HGG, as expected. It is evident that the diffusivity measurements were lower,  $f_{in}$  and cellularity were higher, and  $d$  was lower in the HGG

case compared to LGG. Within the HGG case, heterogeneity was also observed with lower diffusivity, lower  $d$ , and higher  $f_{in}$  and cellularity in the center of the tumor, which corresponded to the slightly elevated intensity in the T1w-enhanced image.

Group differences between LGG and HGG were significant ( $P < 10^{-4}$ ) for all MRI markers ([Figure 2B](#)). Specifically, T1 and T2 relaxation times, ADCs at individual  $t_d$ s,  $D_{ex}$ , and  $d$  were lower in HGG patients compared to LGG, while  $f_{in}$  and cellularity were higher in the HGG group. As a result, all of the MRI markers showed reasonable diagnostic accuracy in differentiating HGG from LGG. The cellularity index achieved the highest AUC of 0.911 and accuracy/sensitivity/specificity of 0.884/0.893/0.878, followed by  $D_{0\text{Hz}}$  and  $D_{33\text{Hz}}$  with AUCs of 0.906 and 0.891, respectively ([Table 1](#)). T1 and T2 relaxation times showed relatively low classification accuracy compared to the dMRI markers with AUCs of 0.847 and 0.861, respectively. We also tested the combinations of

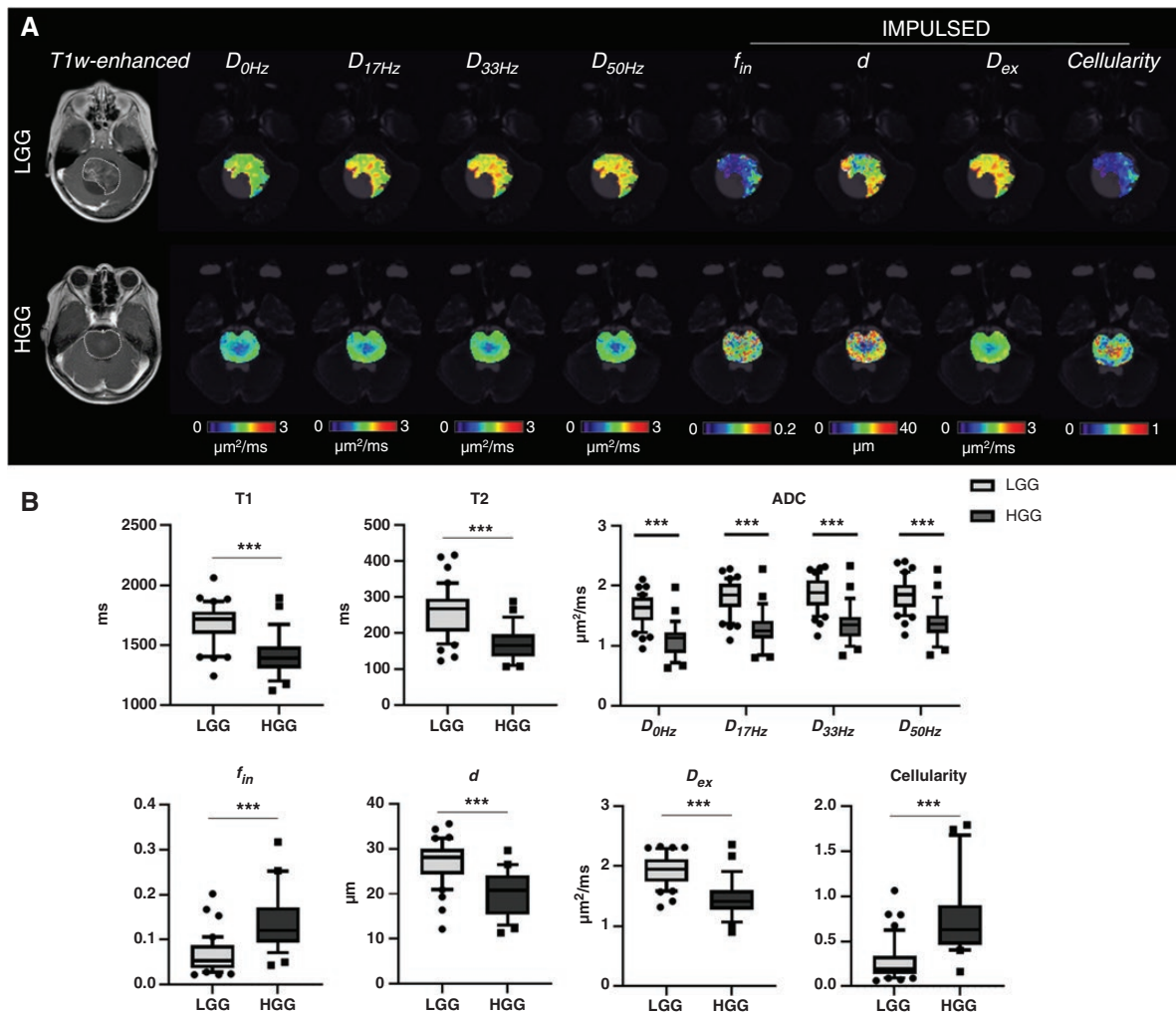


**Figure 2.**  $t_d$ -dMRI-based microstructural mapping for histological grading. (A) T1w-enhanced image, diffusivity maps at each  $t_d$ , and microstructural maps of  $f_{in}$ ,  $d$ ,  $D_{ex}$ , and cellularity estimated from the IMPULSED model in one LGG patient (3-year-old boy, pilocytic astrocytoma, WHO II) and one high-grade glioma (HGG) patient (9-year-old boy, midline glioma, WHO IV). (B) Group differences between LGG and HGG patients for all MRI markers, including T1 and T2 relaxation times, ADCs at individual  $t_d$ s,  $f_{in}$ ,  $d$ ,  $D_{ex}$ , and cellularity. \*\*\*  $P < 10^{-4}$ .

**Table 1.** Diagnostic Performance of the Multi-modal MRI Markers in Differentiating HGG From LGG. Data in the Second Rows are Numbers of Correctly Identified Numbers/Total Number of Patients for Accuracy, Sensitivity, and Specificity. Data in Parenthesis have Bootstrapped 95% Confidence Intervals for AUC. The Cutoffs Between LGG and HGG Groups for Each of the Markers are Also Listed. The Markers With the Highest Performance for Each Evaluation Metric Are Bolded

MRI Marker	Accuracy	Sensitivity	Specificity	AUC	Cutoff
Cellularity	<b>0.8841</b> 61/69	<b>0.8929</b> 25/28	0.8780 36/41	<b>0.9111</b> (0.8393–0.9830)	0.4120
$d$	0.7826 54/69	0.7857 22/28	0.7805 32/41	0.8493 (0.7602–0.9384)	24.20 $\mu\text{m}$
$D_{ex}$	0.8551 59/69	0.8214 23/28	0.8780 36/41	0.8789 (0.7827–0.9752)	1.643 $\mu\text{m}^2/\text{ms}$
$f_{in}$	0.8116 56/69	0.8929 25/28	0.7561 31/41	0.8650 (0.7787–0.9513)	0.08679
$D_{0\text{Hz}}$	0.8696 60/69	0.8214 23/28	0.9024 37/41	0.9059 (0.8254–0.9864)	1.292 $\mu\text{m}^2/\text{ms}$
$D_{17\text{Hz}}$	0.8696 60/69	0.8571 24/28	0.8780 36/41	0.8955 (0.8102–0.9807)	1.459 $\mu\text{m}^2/\text{ms}$
$D_{33\text{Hz}}$	0.8696 60/69	0.7857 22/28	<b>0.9268</b> 38/41	0.8911 (0.8021–0.9801)	1.483 $\mu\text{m}^2/\text{ms}$
$D_{50\text{Hz}}$	0.8696 60/69	0.8214 23/28	0.9024 37/41	0.8780 (0.7847–0.9713)	1.517 $\mu\text{m}^2/\text{ms}$
FA	0.7246 50/69	0.8214 23/28	0.6585 27/41	0.7265 (0.5981–0.8549)	0.2570
AD	0.7681 52/69	0.7857 22/28	0.7561 31/41	0.8127 (0.7092–0.9162)	1.1336 $\mu\text{m}^2/\text{ms}$
RD	0.8551 60/69	0.8571 24/28	0.8537 35/41	0.8685 (0.7784–0.9585)	0.7210 $\mu\text{m}^2/\text{ms}$
T1	0.8116 56/69	0.7857 22/28	0.8293 34/41	0.8467 (0.7454–0.9480)	1514 ms
T2	0.8116 56/69	0.8571 24/28	0.7805 32/41	0.8615 (0.7744–0.9485)	204.0 ms

HGG, high-grade glioma; LGG, low-grade glioma.

these MRI markers but did not find further improvement compared to the single marker of cellularity.

## Molecular Classification

Within the 39 midline glioma patients, we investigated microstructural features in H3K27-altered and wild-type patients. Figure 3A demonstrated representative microstructural maps from a H3K27-wildtype (12 years 11 months old boy, midline glioma in the cerebellar vermis) and a H3K27-altered patient (5 years old girl, midline glioma in the brainstem). The H3K27-altered tumor exhibited clearly reduced ADC,  $D_{ex}$ , and  $d$ , and elevated  $f_{in}$  and cellularity compared to the wildtype midline glioma, with a slight regional heterogeneity, eg, higher malignancy in the left part of the tumor as indicated by the dMRI parametric maps and T1w-enhanced image.

Quantitative analysis revealed significantly reduced T1 and T2 relaxation times ( $P < .01$ ) in the H3K27-altered group compared to the wildtype midline glioma (Figure 3B), but the diagnostic accuracy of T1 and T2 mapping were relatively low with AUCs of 0.821 and 0.808, respectively. The  $t_d$ -dMRI-based parameters showed strong group differences with considerably lower ADCs,  $d$ , and  $D_{ex}$  and elevated

$f_{in}$  and cellularity in the H3K27-altered group (Figure 3B). Particularly, the cell diameter index  $d$  showed the highest discriminant power with an AUC of 0.918 and accuracy/sensitivity/specificity of 0.846/0.950/0.737 (Table 2), which was different from the histological classification where the cellularity was the best.  $D_{17\text{Hz}}$  had the second-to-best performance with an AUC of 0.910 and the other diffusivity metrics had equivalent AUCs of around 0.9. Combinations of  $d$  and  $D_{ex}$  further improved the AUC to 0.929 compared to the single markers.

## Pathological Validation

The nuclei of cells were automatically segmented from the H&E stained sections with cGAN, which revealed different degrees of cell proliferation in LGG and HGG patients (Figure 4A–B). The volume fraction quantified from the segmented nuclei ( $f_{nuclei}$ ) correlated well with the IMPULSED model-derived  $f_{in}$  with a correlation coefficient ( $r$ ) of 0.6996 and  $P < .0001$  in 37 patients (Figure 4C). But the histology-based  $d_{nuclei}$  did not show a significant correlation with IMPULSED-based  $d$ , possibly because the nuclei diameter from histology was not linearly scalable to cell diameter from  $t_d$ -dMRI given the high degree of pleomorphism

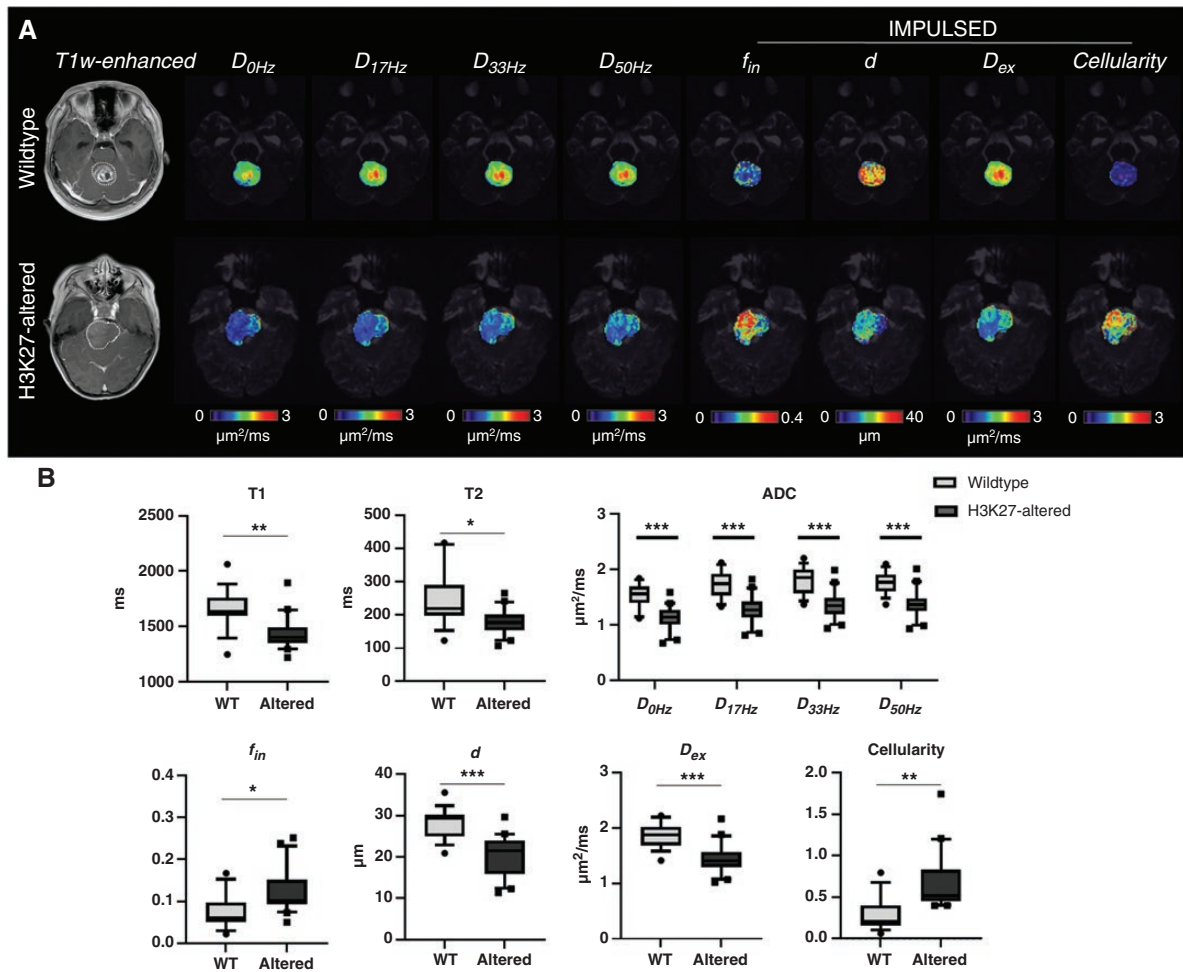


**Figure 3.**  $t_d$ -dMRI based microstructural mapping for classification of H3K27-altered and wildtype midline glioma. (A) T1w-enhanced image, diffusivity maps at each  $t_d$ , and microstructural maps of  $f_{in}$ ,  $d$ ,  $D_{ex}$  and *cellularity* estimated from the IMPULSED model in a wildtype (12 years 11 months old boy, midline glioma in the cerebellar vermis) and a H3K27-altered patient (5-year-old girl, midline glioma in the brainstem). (B) Group differences between H3K27-altered and wildtype midline glioma patients for all MRI markers, including T1 and T2 relaxation times, ADCs at individual  $t_d$ ,  $f_{in}$ ,  $d$ ,  $D_{ex}$  and *cellularity*. \*  $P < 10^{-2}$ , \*\*  $P < 10^{-3}$ , \*\*\*  $P < 10^{-4}$ .

in glioma.<sup>34</sup> Nevertheless, the estimated cell diameters ( $24.27 \pm 5.90 \mu\text{m}$ ) were consistent with the previous studies that reported the glioma cell size around  $20 \mu\text{m}$ .<sup>35,36</sup>

## Discussion

As pointed out by the WHO 2021 guideline, the combination of histological and molecular classification is essential for precise prognosis and optimal treatment plans in CNS tumor patients. Here, we designed a prospective study to investigate the clinical utility of newly proposed cell microstructural markers based on the  $t_d$ -dMRI theory for both histological and molecular identification in pediatric gliomas. Our preliminary results illustrated that the cellularity index had a superior performance in diagnosing LGG and HGG, while the cell diameter index showed high discriminative power in separating H3K27-altered and

wildtype midline glioma, indicating promising values of these noninvasive microstructural features in pediatric gliomas. Particularly, the fact that different histological and molecular subtypes exhibited unique microstructural properties (cellularity or cell size) suggested the importance of having specific pathological indicators, instead of the simple ADC measurement, and  $t_d$ -dMRI could accurately provide such information.

Despite the importance of molecular markers, histological grading still plays an indispensable role in the clinical management of pediatric gliomas. The general consensus is that HGG must always be operated on except for surgical contradictions, along with adjuvant radiotherapy and/or chemotherapy; while the treatment strategy for LGG remains controversial given the balance between treatment efficacy and post-treatment quality of life in pediatric patients.<sup>37</sup> Therefore, timely and accurate histological grading of the tumor malignancy provides important

**Table 2.** Diagnostic Performance of the Multi-modal MRI Markers in Differentiating H3K27-altered From Wildtype DMG Patients. Data in the Second Rows are Numbers of Correctly Identified Numbers/Total Number of Patients for Accuracy, Sensitivity, and Specificity. Data in Parenthesis have Bootstrapped 95% Confidence Intervals for AUC. The Cutoffs Between H3K27-altered and Wildtype Groups for Each of the Markers are Also Listed. The Markers With the Highest Performance for Each Evaluation Metric are Bolded

MRI Marker	Accuracy	Sensitivity	Specificity	AUC	Threshold
Cellularity	0.8718 34/39	<b>1.0000</b> 20/20	0.7368 14/19	0.9132 (0.8181–1.000)	0.3641
$d$	0.8718 34/39	0.9000 18/20	0.8421 16/19	<b>0.9184</b> (0.8330–1.000)	24.89 $\mu\text{m}$
$D_{ex}$	<b>0.8974</b> 35/39	0.9000 18/20	0.8947 17/19	0.9026 (0.7959–1.000)	1.643 $\mu\text{m}^2/\text{ms}$
$f_{in}$	0.7692 30/39	0.9000 18/20	0.6316 12/19	0.7842 (0.6376–0.9303)	0.08679
$D_{0\text{Hz}}$	0.8718 34/39	0.9500 19/20	0.7895 15/19	0.9053 (0.8111–0.9994)	1.392 $\mu\text{m}^2/\text{ms}$
$D_{17\text{Hz}}$	0.8718 34/39	0.9000 18/20	0.8421 16/19	0.9105 (0.8218–0.9993)	1.486 $\mu\text{m}^2/\text{ms}$
$D_{33\text{Hz}}$	0.8718 34/39	0.8500 17/20	0.8947 17/19	0.9026 (0.8051–1.000)	1.497 $\mu\text{m}^2/\text{ms}$
$D_{50\text{Hz}}$	0.8462 33/39	0.7500 15/20	<b>0.9474</b> 18/19	0.8868 (0.7782–0.9955)	1.471 $\mu\text{m}^2/\text{ms}$
FA	0.7436 29/39	1.0000 20/20	0.4737 9/19	0.7763 (0.6216–0.9311)	0.2349
AD	0.7436 29/39	0.7500 15/20	0.7368 14/19	0.7684 (0.6166–0.9202)	1.136 $\mu\text{m}^2/\text{ms}$
RD	0.8718 34/39	0.8500 17/20	0.8947 17/19	0.8868 (0.7793–0.9944)	0.7059 $\mu\text{m}^2/\text{ms}$
T1	0.8462 33/39	0.8500 17/20	0.8421 16/19	0.8211 (0.6779–0.9642)	1562 ms
T2	0.7949 31/39	0.8500 17/20	0.7368 14/19	0.8079 (0.6653–0.9505)	204.0 ms

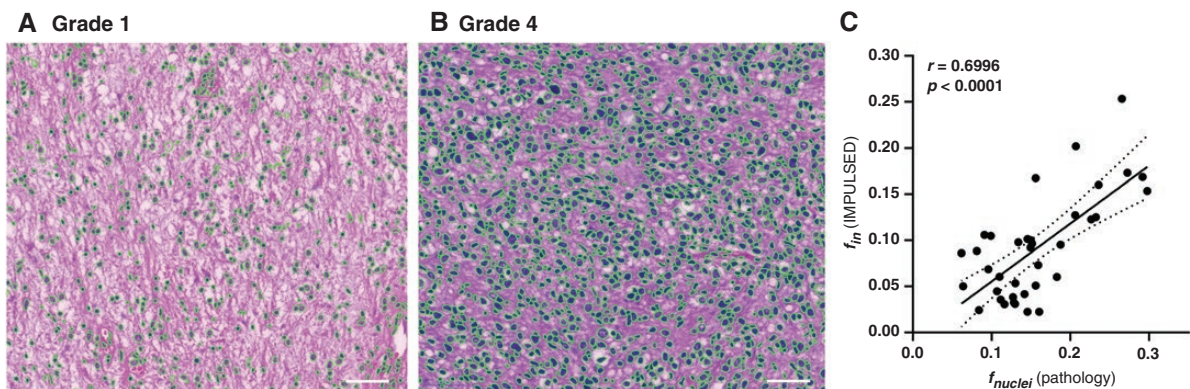


**Figure 4.** Pathological validation of  $t_d$ -MRI microstructural mapping results. (A–B) Typical segmented hematoxylin and eosin (H&E)-stained slices ( $\times 30$  magnification, scale bar: 50  $\mu\text{m}$ ) from the biopsy of a LGG (a, 2 years and 11 months old boy, pilocytic astrocytoma in the cerebellum, grade 1) and a high-grade glioma (b, 10 years and 3 months old girl, midline glioma in the brainstem, grade 4) patients. (C) Correlation between  $f_{in}$  from IMPULSED model and  $f_{nuclei}$  from the pathological images in 37 patients.

first-hand information. Several studies have investigated the use of advanced MRI in grading pediatric gliomas. A recent study by Yao et al. reported an accuracy of 89.5% and

86.9% using ADC and NAA/Cho from MR spectroscopy in a cohort of 143 LGG and 66 HGG pediatric patients.<sup>10</sup> Gupta et al. tested dynamic contrast-enhanced (DCE) in a cohort



of 64 pediatric tumor patients and found the relative cerebral blood volume could separate HGG from LGG with 88.6% sensitivity and 65% specificity,<sup>38</sup> although DCE is not the standard way to calculate cerebral blood volume, it is still feasibly after the correction of the leakage effect. Zhang et al. employed amide proton transfer (APT) MRI in 48 pediatric glioma patients and obtained an AUC of 0.86 in differentiating LGG versus HGG.<sup>39</sup> In our study cohort, the microstructural index of cellularity achieved an AUC of 0.911, outperforming the conventional dMRI measurements and also T1/T2 mappings. The findings corresponded well with the characteristic cell proliferation in HGG that led to elevated cellularity.<sup>28</sup> It was also assuring from the histological validation that the  $t_d$ -dMRI-based estimation of microstructural properties agreed well with the ground truth. Therefore, by pinpointing the microstructural features of tumor pathology, we may further enhance the accuracy of noninvasive identification of histological grade.

On the other hand, midline glioma, as an inoperable category in pediatric glioma, is known to have a highly complex and variable radiological appearance depending on its molecular subtypes.<sup>40</sup> Conventional MRI has limited power in predicting H3K27 alteration in midline glioma patients.<sup>41,42</sup> The applications of advanced molecular imaging<sup>12,43</sup> or advanced analytical approaches including radiomics and machine-learning methods<sup>44–46</sup> showed promising improvement. Zhuo et al. reported that the radiomics measures from APT-weighted imaging provided an accuracy of 0.88 in identifying H3K27M-mutant brainstem glioma.<sup>43</sup> Su et al. utilized radiological features from FLAIR images along with a machine-learning model and achieved AUCs of 0.85 in the testing set from a total of 100 midline glioma patients.<sup>44</sup> A most recent study used a combination of clinical and radiological features from 107 HGG patients and reached an AUC of 0.92 for predicting H3K27M mutation in the testing data.<sup>45</sup> However, sophisticated radiomics and machine-learning models are known to have limited generalizability and easily get overfitted without a large number of samples. Here we used the simple ROI means to evaluate the native performance of each MRI marker. The cell diameter index performed best in this task with the highest AUC of 0.918, despite the relatively small sample size ( $n = 39$ ). Despite the histopathological spectrum of H3K27 alteration,<sup>29</sup> the H3K27-altered group had a significantly lower cell diameter compared to wildtype midline glioma. One common histologic feature of H3K27-alteration is that the tumor cells exhibit pilocytic astrocytic morphology with piloid appearance,<sup>29,47</sup> which may lead to a reduced diameter measurement from the  $t_d$ -dMRI model.

Interestingly, we noticed some of the H3K27-altered midline gliomas exhibited low histological characteristics. We further looked at the microstructural features of these cases and found relatively low cellularity in these patients but their cell diameter was in the range of the H3K27-altered group (Supplementary Figure S3). Therefore, it is important to have a comprehensive picture of the tumor microstructure for accurate histological and molecular identification. In addition, correlation analysis between ADC and the microstructural markers showed relatively weak and nonlinear correlations (Supplementary Figure S4), indicating the different measurements may provide

complementary information. Indeed, we found further improvement of H3K27 diagnosis was achieved by combining cell diameter and diffusivity markers.

Notably, H3K27-altered midline glioma is characterized mainly by H3K27M mutation, EZHIP-overexpression, and others.<sup>7</sup> In company with the primary genomic alternation, additional recurrent defects include inactivation of the p53 and Rb pathways, activation mutations of ACVR1, and alternations of genes in the receptor tyrosine kinase pathway (eg, PDGFRA, EGFR, FGFR1, and PI3KCA).<sup>48,49</sup> Hence, it is very likely that H3K27-alteration collaborates with other “cooperating mutations” on disease development and progression. It would be interesting to further group patients according to the histone alterations and genetic co-mutations for their microstructural signatures with the  $t_d$ -dMRI model, given full sequencing data.

The current study has several limitations. Our sample size was not large enough ( $n = 69$  for histological grading and 39 for molecular classification), which limited the diagnostic accuracy. Larger sample sizes and ideally a multisite study are needed in the future to confirm the clinical value of the proposed microstructural markers. Secondly, for histological validation, we could not have an exact spatial match between the MRI-based tumor ROI and biopsy sample. Since it is extremely difficult to dissect the intact tumor from brain glioma patients, we assumed the biopsy was representative of the tumor pathology. In addition, we only presented the ROI average for direct assessment of the diagnostic accuracy of each MRI marker. The use of radiomics for higher-order features may further improve the discriminative power, given sufficient sample size. Also, the combination of  $t_d$ -dMRI with other imaging modalities, such as molecular imaging or perfusion MRI, may also enhance our ability to noninvasively predict tumor phenotypes and genotypes.

## Supplementary Material

Supplementary material is available online at *Neuro-Oncology* (<http://neuro-oncology.oxfordjournals.org/>).

## Keywords

diffusion MRI | microstructure | pediatric glioma | histological grading | H3K27-altered

## Funding

This work was supported by the Ministry of Science and Technology of the People's Republic of China (2018YFE0114600, 2021YFC2701901), the National Natural Science Foundation of China (81971606, 82122032), and the Science and Technology Department of Zhejiang Province (202006140, 2022C03057).

## Authorship Statement

Investigation, experiment, data analysis, and manuscript preparation: Hongxi Zhang and Kuiyuan Liu; Data analysis and validation: Ruichen Ba, Zelin Zhang, and Yi Zhang; Patient recruitment, experiment, and analysis: Ye Chen, Weizhong Gu, and Zhipeng Shen; Conceptualization, investigation, data resource, experiment, analysis, and manuscript preparation: Dan Wu, Junfen Fu, and Qiang Shu.

## Conflict of Interest

The authors declare no potential conflicts of interest.

## References

- Ward E, DeSantis C, Robbins A, Kohler B, Jemal A. Childhood and adolescent cancer statistics, 2014. *CA Cancer J Clin*. 2014;64(2):83–103.
- Armstrong GT, Liu Q, Yasui Y, et al. Long-term outcomes among adult survivors of childhood central nervous system malignancies in the childhood cancer survivor study. *J Natl Cancer I*. 2009;101(13):946–958.
- Ryall S, Tabori U, Hawkins C. Pediatric low-grade glioma in the era of molecular diagnostics. *Acta Neuropathol Commun*. 2020;8(1):1–22.
- Qaddoumi I, Sultan L, Gajjar A. Outcome and prognostic features in pediatric gliomas a review of 6212 cases from the Surveillance, epidemiology, and end results database. *Cancer*. 2009; 115(24):5761–5770.
- Hoffman LM, van Zanten SEMV, Colditz N, et al. Clinical, radiologic, pathologic, and molecular characteristics of long-term survivors of diffuse intrinsic pontine glioma (DIPG): a collaborative report from the International and European Society for Pediatric Oncology DIPG Registries. *J Clin Oncol*. 2018;36(19):1963–1972.
- Karremann M, Gielen GH, Hoffmann M, et al. Diffuse high-grade gliomas with H3 K27M mutations carry a dismal prognosis independent of tumor location. *Neuro Oncol*. 2018;20(1):123–131.
- Louis DN, Perry A, Wesseling P, et al. The 2021 WHO classification of tumors of the central nervous system: a summary. *Neuro Oncol*. 2021;23(8):1231–1251.
- Argersinger DP, Rivas SR, Shah AH, Jackson S, Heiss JD. New developments in the pathogenesis, therapeutic targeting, and treatment of H3K27M-mutant diffuse midline glioma. *Cancers*. 2021;13(21):5280.
- Osada Y, Saito R, Shibahara I, et al. H3K27M and TERT promoter mutations are poor prognostic factors in surgical cases of adult thalamic high-grade glioma. *Neurooncol Adv*. 2021;3(1):vdab038.
- Yao R, Cheng AL, Liu ML, et al. The diagnostic value of apparent diffusion coefficient and proton magnetic resonance spectroscopy in the grading of pediatric gliomas. *J Comput Assist Tomo*. 2021;45(2):269–276.
- Wang QP, Lei DQ, Yuan Y, Xiong NX. Accuracy of ADC derived from DWI for differentiating high-grade from low-grade gliomas Systematic review and meta-analysis. *Medicine*. 2020;99(8):e19254.
- Piccardo A, Tortora D, Mascelli S, et al. Advanced MR imaging and (18)F-DOPA PET characteristics of H3K27M-mutant and wild-type pediatric diffuse midline gliomas. *Eur J Nucl Med Mol Imaging*. 2019;46(8):1685–1694.
- Jiang H, Yang K, Ren X, et al. Diffuse midline glioma with H3 K27M mutation: a comparison integrating the clinical, radiological, and molecular features between adult and pediatric patients. *Neuro Oncol*. 2020;22(5):e1–e9.
- Kathrani N, Chauhan RS, Kotwal A, et al. Diffusion and perfusion imaging biomarkers of H3 K27M mutation status in diffuse midline gliomas. *Neuroradiology*. 2022;64(8):1519–1528.
- Wang Y, Wang Q, Haldar JP, et al. Quantification of increased cellularity during inflammatory demyelination. *Brain*. 2011;134(Pt 12):3590–3601.
- Zhang H, Schneider T, Wheeler-Kingshott CA, Alexander DC. NODDI: practical in vivo neurite orientation dispersion and density imaging of the human brain. *Neuroimage*. 2012;61(4):1000–1016.
- Palombo M, Ianus A, Guerreri M, et al. SANDI: a compartment-based model for non-invasive apparent soma and neurite imaging by diffusion MRI. *Neuroimage*. 2020;215:116835.
- Novikov DS, Fieremans E, Jespersen SN, Kiselev VG. Quantifying brain microstructure with diffusion MRI: theory and parameter estimation. *NMR Biomed*. 2019;32(4):e3998.
- Gore JC, Xu JZ, Colvin DC, et al. Characterization of tissue structure at varying length scales using temporal diffusion spectroscopy. *NMR Biomed*. 2010;23(7):745–756.
- Jiang XY, Li H, Xie JP, et al. In vivo imaging of cancer cell size and cellularity using temporal diffusion spectroscopy. *Magn Reson Med*. 2017;78(1):156–164.
- Xu J, Jiang X, Li H, et al. Magnetic resonance imaging of mean cell size in human breast tumors. *Magn Reson Med*. 2020;83(6):2002–2014.
- Panagiotaki E, Walker-Samuel S, Siow B, et al. Noninvasive quantification of solid tumor microstructure using VERDICT MRI. *Cancer Res*. 2014;74(7):1902–1912.
- Reynaud O, Winters KV, Hoang DM, et al. Pulsed and oscillating gradient MRI for assessment of cell size and extracellular space (POMACE) in mouse gliomas. *NMR Biomed*. 2016;29(10):1350–1363.
- Reynaud O. Time-dependent diffusion MRI in cancer: tissue modeling and applications. *Front Phys*. 2017;5:58.
- Iima M, Yamamoto A, Kataoka M, et al. Time-dependent diffusion MRI to distinguish malignant from benign head and neck tumors. *J Magn Reson Imaging*. 2019;50(1):88–95.
- Wu D, Jiang K, Li H, et al. Time-dependent diffusion MRI for quantitative microstructural mapping of prostate cancer. *Radiology*. 2022;211180(3):578–587.
- Chatterjee A, Oto A. Prostate tissue microstructural estimates using time-dependent diffusion MRI. *Radiology*. 2022;220056(3):588–589.
- Gladson CL, Prayson RA, Liu WM. The pathobiology of glioma tumors. *Annu Rev Pathol-Mech*. 2010;5:33–50.
- Solomon DA, Wood MD, Tihan T, et al. Diffuse midline gliomas with histone H3-K27M mutation: a series of 47 cases assessing the spectrum of morphologic variation and associated genetic alterations. *Brain Pathol*. 2016;26(5):569–580.
- Gao FS, Shen XX, Zhang HX, et al. Feasibility of oscillating and pulsed gradient diffusion MRI to assess neonatal hypoxia-ischemia on clinical systems. *J Cerebr Blood F Met*. 2021;41(6):1240–1250.
- Denkleef JJEI, Cuppen JJM. Rlsq - T1, T2, and rho-calculations, combining ratios and least-squares. *Magn Reson Med*. 1987; 5(6):513–524.
- Stepisnik J. Time-dependent self-diffusion by NMR spin-echo. *Physica B*. 1993;183(4):343–350.
- Isola P, Zhu JY, Zhou TH, Efros AA. Image-to-image translation with conditional adversarial networks. *Proc Cyp IEEE*. 2017:5967–5976.
- Urbańska K, Sokołowska J, Szmidi M, Sysa P. Glioblastoma multiforme - an overview. *Contemp Oncol (Pozn)*. 2014;18(5):307–312.
- Giuliano KA. Dissecting the individuality of cancer cells: the morphological and molecular dynamics of single human glioma cells. *Cell Motility*. 1996;35(3):237–253.
- Tamaki M, McDonald W, Amberger VR, Moore E, DelMaestro RF. Implantation of C6 astrocytoma spheroid into collagen type I gels:

- invasive, proliferative, and enzymatic characterizations. *J Neurosurg.* 1997;87(4):602–609.
37. van den Bent MJ, Snijders TJ, Bromberg JE. Current treatment of low grade gliomas. *Memo.* 2012;5(3):223–227.
  38. Gupta PK, Saini J, Sahoo P, et al. Role of dynamic contrast-enhanced perfusion magnetic resonance imaging in grading of pediatric brain tumors on 3T. *Pediatr Neurosurg.* 2017;52(5):298–305.
  39. Zhang HX, Yong XW, Ma XH, et al. Differentiation of low- and high-grade pediatric gliomas with amide proton transfer imaging: added value beyond quantitative relaxation times. *Eur Radiol.* 2021;31(12):9110–9119.
  40. Aboian MS, Solomon DA, Felton E, et al. Imaging characteristics of pediatric diffuse midline gliomas with histone H3 K27M mutation. *Am J Neuroradiol.* 2017;38(4):795–800.
  41. Hohm A, Karremann M, Gielen GH, et al. Magnetic resonance imaging characteristics of molecular subgroups in pediatric H3 K27M mutant diffuse midline glioma. *Clin Neuroradiol.* 2022;32(1):249–258.
  42. Aboian MS, Tong E, Solomon DA, et al. Diffusion characteristics of pediatric diffuse midline gliomas with histone H3-K27M mutation using apparent diffusion coefficient histogram analysis. *Am J Neuroradiol.* 2019;40(11):1804–1810.
  43. Zhuo Z, Qu L, Zhang P, et al. Prediction of H3K27M-mutant brainstem glioma by amide proton transfer-weighted imaging and its derived radiomics. *Eur J Nucl Med Mol Imaging.* 2021;48(13):4426–4436.
  44. Su X, Chen N, Sun H, et al. Automated machine learning based on radiomics features predicts H3 K27M mutation in midline gliomas of the brain. *Neuro Oncol.* 2020;22(3):393–401.
  45. Wu CQ, Zheng H, Li JN, et al. MRI-based radiomics signature and clinical factor for predicting H3K27M mutation in pediatric high-grade gliomas located in the midline of the brain. *Eur Radiol.* 2022;32(3):1813–1822.
  46. Pan CC, Liu J, Tang J, et al. A machine learning-based prediction model of H3K27M mutations in brainstem gliomas using conventional MRI and clinical features. *Radiother Oncol.* 2019;130:172–179.
  47. Orillac C, Thomas C, Dastagirzada Y, et al. Pilocytic astrocytoma and glioneuronal tumor with histone H3 K27M mutation. *Acta Neuropathol Commun.* 2016;4:1–4.
  48. Buczkowicz P, Hoeman C, Rakopoulos P, et al. Genomic analysis of diffuse intrinsic pontine gliomas identifies three molecular subgroups and recurrent activating ACVR1 mutations. *Nat Genet.* 2014;46(5):451–456.
  49. Wu G, Diaz AK, Paugh BS, et al. The genomic landscape of diffuse intrinsic pontine glioma and pediatric non-brainstem high-grade glioma. *Nat Genet.* 2014;46(5):444–450.